J. Fluid Mech. (2025), *vol.* 1008, A6, doi:10.1017/jfm.2025.137

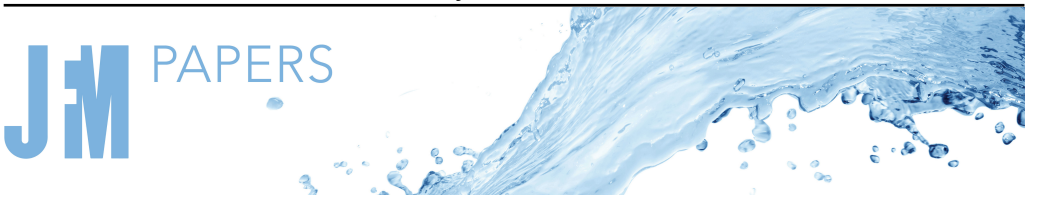

Attenuation of turbulence in a periodic cube by anisotropic solid particles

Hideto Awai[1], **Yutaro Motoori**[1] **and Susumu Goto**[1]

[1]Graduate School of Engineering Science, Osaka University, 1-3 Machikaneyama, Toyonaka, Osaka 560-8531, Japan

Corresponding authors: Yutaro Motoori, y.motoori.es@osaka-u.ac.jp; Susumu Goto, s.goto.es@osaka-u.ac.jp

(Received 6 July 2024; revised 23 January 2025; accepted 24 January 2025)

We conduct direct numerical simulations (DNS) to investigate the attenuation of turbulence in a periodic cube due to the addition of prolate spheroidal solid particles. Even with a dilute volume fraction of $O(10^{-2})$, particles can drastically attenuate the turbulence. Our DNS show that the turbulent kinetic energy reduces more significantly when the particles' Stokes number is larger, size is smaller or aspect ratio is larger. We can explain these results based on the formula proposed by Oka and Goto (2022 *J. Fluid Mech.* **949**, A45), which relates the turbulence attenuation rate to the energy dissipation rate ϵ_p around particles. More precisely, under the condition that the volume fraction of particles is fixed, ϵ_p is larger when the Stokes number and, therefore, the relative velocity between fluid and particles are larger, the particle size is smaller or the aspect ratio is larger. These results also imply that the rotation of the anisotropic particles plays only a limited role in the attenuation of turbulence when the Stokes number of particles is sufficiently large, because the main cause of the attenuation is the relative translational velocity between fluid and particles.

Key words: turbulent flows, multiphase and particle-laden flows

1. Introduction

By adding a small amount of solid particles to turbulent flows, we can drastically modulate turbulence. This interesting phenomenon has been well known since the last century when seminal experiments of particle-laden pipe flow (Tsuji & Morikawa 1982) and free jet (Levy & Lockwood 1981) were conducted. Gore & Crowe (1989) summarised experimental data at that time to conclude that the particle size D compared with the

integral length L (i.e. the size of the largest eddies) of turbulence is the important parameter and turbulence can be augmented (or attenuated) when D/L is larger (or smaller) than 0.1. The target of the present study is the attenuation of turbulence by particles smaller than L.

Gore & Crowe (1989) already mentioned the mechanism of the turbulence attenuation, where small particles acquire the kinetic energy of turbulence from the most energetic (i.e. the largest) eddies. However, the physical mechanism of turbulence modulation is still under debate because it is difficult to draw a concrete picture of the complex phenomenon only by experiments, and because it is also difficult to conduct parametric study in laboratory. In contrast, since the seminal study by Elghobashi (1994), direct numerical simulations (DNS) of multi-phase turbulence have been developing to be powerful enough for effective parameter surveys. Therefore, the combination of state-of-the-art measurements and DNS is rapidly advancing the understanding of turbulence modulation by solid particles (Balachandar & Eaton 2010; Brandt & Coletti 2022). Even if we only look at the literature in the simplest case, i.e. the modulation of turbulence in a periodic cube, which is also the target of the present study, a number of DNS were conducted (ten Cate *et al.* 2004; Homann & Bec 2010; Yeo *et al.* 2010; Lucci, Ferrante & Elghobashi 2010, 2011; Gao, Li & Wang 2013; Wang *et al.* 2014; Schneiders, Meinke & Schröder 2017; Oka & Goto 2022; Peng, Sun & Wang 2023; Su *et al.* 2023; Cannon, Olivieri & Rosti 2024; Chiarini, Cannon & Rosti 2024) to reveal the statistics and dynamics of particle-turbulence interactions. Among these studies, it is particularly important to note the observation made by ten Cate *et al.* (2004), Yeo *et al.* (2010), Gao *et al.* (2013) and Wang *et al.* (2014) that, when turbulence is attenuated, the energy spectrum is attenuated (and augmented) in the wavenumber range corresponding to length scales larger (and smaller) than particles, because this is consistent with the physical mechanism of turbulence attenuation examined in the present article; namely, particles acquire the energy from the largest eddies and dissipate it in the shedding particle-size vortices around them.

Thanks to parametric studies by DNS and accumulations of experimental data, the condition of turbulence attenuation (or augmentation) was proposed in terms of not only the normalised particle size D/L (Gore & Crowe 1989), but also other parameters such as the volume fraction Λ, the mass loading and the Stokes number,

$$St = \frac{\tau_p}{T}\,, \tag{1.1}$$

where τ_p and T denote the particle velocity relaxation time due to the Stokes drag and the turnover time of the largest vortices, respectively. For example, Tanaka & Eaton (2008) proposed a dimensionless number and even recently, Peng *et al.* (2023) also suggested another parametrisation for the turbulence modulation. Note that in the present study, we define the Stokes number (1.1) by T because it quantifies the particles' ability to follow the most energetic motion in turbulence, but other definitions of the Stokes number are sometimes used (see e.g. Bordoloi & Variano 2017). Note also that the target of the present study is turbulence modulation by particles much heavier than carrier fluid, where added mass effects are negligible.

We also investigated this issue by DNS of the attenuation of turbulence in a periodic cube due to spherical particles (Oka & Goto 2022) to show that the turbulent kinetic energy K' can be reduced by approximately half, even if the volume fraction Λ is as small as 8×10^{-3}, if St is sufficiently larger than 1 and D is smaller than L. This implies that both D/L and St are important parameters. We also demonstrated that when St is large enough, particle-size vortices are shed from particles because of large-enough relative

velocity between fluid and particles, and then the energy which the particles acquire from the largest eddies is dissipated in these shedding vortices. Then, we showed that we can estimate the attenuation rate,

$$\mathcal{A} = 1 - \frac{K'}{K'_0}\,, \tag{1.2}$$

where K'_0 is the average turbulent kinetic energy of the single-phase flow, by considering the average energy dissipation rate ϵ_p in the wake. More precisely, the average energy input rate ϵ_0, which is assumed to be the same as in the single-phase turbulence, is the sum of the average flux ϵ_c of the energy cascade in the particle-laden turbulence and the average dissipation rate ϵ_p around particles:

$$\epsilon_0 = \epsilon_c + \epsilon_p\,. \tag{1.3}$$

Since ϵ_0 and ϵ_c are the energy flux in the single- and multi-phase flows, respectively, we can estimate them as

$$\epsilon_0 = C_\epsilon \frac{(K_0 + K'_0)^{3/2}}{L_0} \quad \text{and} \quad \epsilon_c = C_\epsilon \frac{(K_0 + K')^{3/2}}{L_0} \tag{1.4}$$

by the dissipation law of Taylor (1935). Here, K_0 and L_0 denote the kinetic energy of mean flow and integral length in the single-phase flow, respectively, which are assumed to be the same as those in the particle-laden flow (see the verification of these assumptions in Appendix A). The coefficient C_ϵ is the dissipation coefficient, which depends on flow (Goto & Vassilicos 2009). Substituting (1.4) into (1.3), we can relate $\mathcal{A}$ to ϵ_p as

$$1 - \left(1 - \frac{\mathcal{A}}{1+\alpha}\right)^{3/2} = \frac{\epsilon_p}{\epsilon_0} \tag{1.5}$$

with α being defined as the ratio K_0/K'_0 of the kinetic energy of mean flow to the turbulent kinetic energy in the single-phase flow. Oka & Goto (2022) numerically verified (1.5) by estimating the energy dissipation rate around the particles as

$$\epsilon_p^\dagger = C_p \Lambda \frac{\langle \Delta u^3 \rangle_p}{D}\,, \tag{1.6}$$

where Δu is the relative velocity between fluid and particles, C_p is a constant of $O(1)$, and $\langle\,\cdot\,\rangle_p$ denotes the average over particles and time. The superscript dagger of $\epsilon_p^\dagger$ indicates a theoretical expression (1.6) for ϵ_p. Although the physical picture shown here is based on the classical view described in the second paragraph of this section, the crucial point to derive (1.5) is that we consider the change in the cascading energy flux. Recently, Balachandar, Peng & Wang (2024) further developed this picture towards the subgrid modelling of particle-laden turbulence.

Although Oka & Goto (2022) numerically demonstrated that (1.5) can accurately estimate the attenuation rate $\mathcal{A}$, (1.2), this demonstration was made only for spherical particles. However, it is known that anisotropic particles sometimes more effectively modify turbulence than spherical ones (Voth & Soldati 2017, § 6.2). For example, Paschkewitz *et al.* (2004) showed by DNS with a constitutive equation that rigid fibres can significantly reduce the drag of turbulent channel flow. Many other researchers also investigated the issue of turbulence attenuation and turbulent drag reduction due to anisotropic particles by DNS (Eshghinejadfard, Hosseini & Thévenin 2017; Ardekani & Brandt 2019; Schneiders *et al.* 2019; Wang, Xu & Zhao 2021; Olivieri, Cannon & Rosti 2022; Cannon *et al.* 2024) and experiments (Ljus, Johansson & Almstedt 2002; Bellani

et al. 2012; Capone, Romano & Soldati 2015). As a study related to the present one, Zhao, George & van Wachem (2015) numerically showed that turbulence is more significantly attenuated with anisotropic particles with larger St and larger aspect ratios. Mandø (2009) also examined, by experiments, the modulation of turbulent jet by particles with different shapes and they observed that for a common equivalent diameter,

$$D_* = (6V/\pi)^{1/3}\,, \tag{1.7}$$

where V is the volume of a particle, anisotropic particles (disks and spheroids) attenuate turbulence intensity more than spherical ones.

These previous studies motivate us to investigate the effects of particle shape in turbulence attenuation. However, to systematically investigate the effects, we must examine cases with different shapes of particles under each condition of particles (i.e. Λ, D_*/L and St) and flow (i.e. boundary conditions and the Reynolds number). Thus, in the present study, we restrict ourselves in the case where the particle shape is prolate spheroidal and turbulence is in a triply periodic domain without walls. More concretely, we conduct DNS with different values of D_*/L, St and the aspect ratio χ of prolate spheroidal particles for a fixed value of the volume fraction Λ and the Reynolds number of turbulence. Then, we demonstrate that the above-mentioned physical mechanism of turbulence attenuation is valid even for the anisotropic particles and the estimation (1.5) of $\mathcal{A}$ in terms of ϵ_p holds. We also generalise (1.6) for ϵ_p around anisotropic particles.

2. Direct numerical simulation

2.1. *Numerical method*

We conduct DNS of turbulence with solid prolate spheroids in a periodic cube using the same numerical code used in our previous study (Fujiki *et al*. 2024), in the appendix of which we showed the validation of the code. Here, we briefly describe the numerical method.

First, for fluid motion, we suppose that it is governed by the Navier–Stokes equation,

$$\frac{\partial \boldsymbol{u}}{\partial t} + \boldsymbol{u}\cdot\boldsymbol{\nabla}\boldsymbol{u} = -\frac{1}{\rho_f}\boldsymbol{\nabla} p + \nu\boldsymbol{\nabla}^2\boldsymbol{u} + \boldsymbol{f} + \boldsymbol{f}^{\leftarrow p}, \tag{2.1}$$

and the continuity equation,

$$\boldsymbol{\nabla}\cdot\boldsymbol{u} = 0, \tag{2.2}$$

for an incompressible fluid. Here, $\boldsymbol{u}(\boldsymbol{x}, t)$ is the velocity field at position $\boldsymbol{x}$ and time t, $p(\boldsymbol{x}, t)$ is the pressure field, and ρ_f and ν are the fluid mass density and kinematic viscosity, respectively. In (2.1), $\boldsymbol{f}(\boldsymbol{x})$ is an external steady force, which is expressed as

$$\boldsymbol{f} = (-\sin x \cos y, +\cos x \sin y, 0) \tag{2.3}$$

(Goto, Saito & Kawahara 2017; Oka & Goto 2022), and $\boldsymbol{f}^{\leftarrow p}(\boldsymbol{x}, t)$ is the force due to particles. Using the simplified mark and cell (SMAC) method, we numerically solve (2.1) and (2.2) under periodic boundary conditions in a cube with side $L_{box} = 2\pi$). The spatial derivatives are evaluated using the second-order central difference method. The convection and viscous terms are temporally integrated using the second-order Adams–Bashforth method and Crank–Nicholson method, respectively.

Table 1 lists the parameters such as the number N^3 of grid points for DNS and statistics of the simulated turbulence. Here, we have evaluated the integral length as $L = 3\pi \int_0^\infty k^{-1}E(k)\mathrm{d}k/4\int_0^\infty E(k)\mathrm{d}k$, where $E(k)$ is the temporally averaged energy

	N^3	ν	R_λ	L_{box}/L	L/η	$\eta/\Delta x$	c
RUN256	256^3	8×10^{-3}	47	5.4	47	1.0	6.3×10^{-2}
RUN384	384^3	8×10^{-3}	47	5.3	48	1.5	6.4×10^{-2}

Table 1. Parameters and statistics of the single-phase turbulence. We have taken temporal averages over approximately $250T$ with $T = L/u'$ being the integral time. Here, R_λ, L and η are the Taylor-length-based Reynolds number, integral length and Kolmogorov length, respectively; and $c = u'\Delta t/\Delta x$ is the CFL number defined by the fluctuating velocity u', the grid width $\Delta x = L_{box}/N$ and the time increment Δt for the temporal integration.

spectrum of turbulence, and the Taylor length as $\lambda = \sqrt{10\nu K'/\epsilon}$, where

$$K' = \frac{1}{2}\overline{\langle |\boldsymbol{u}(\boldsymbol{x},t) - \boldsymbol{U}(\boldsymbol{x})|^2\rangle} \qquad \left(\boldsymbol{U}(\boldsymbol{x}) = \overline{\boldsymbol{u}(\boldsymbol{x},t)}\right) \tag{2.4}$$

is the average turbulent kinetic energy per unit mass and ϵ is its dissipation rate. Here, $\langle\,\cdot\,\rangle$ and $\overline{\cdot}$ denote the spatial and temporal averages, respectively. Then, we have evaluated the Taylor-length-based Reynolds number as $R_\lambda = u'\lambda/\nu$ with $u' = \sqrt{2K'/3}$ and the Kolmogorov length as $\eta = \epsilon^{-1/4}\nu^{3/4}$. In table 1, we also list the Courant–Friedrich–Lewy (CFL) number, which we have set sufficiently smaller than unity for numerical stability.

Next, we describe the numerical method to simulate the motion of spheroidal particles with mass density ρ_p, major radius a and minor radius b. Particle's velocity $\boldsymbol{v}_p(t)$ and angular velocity $\boldsymbol{\omega}_p(t)$ obey Newton's equations of motion,

$$m\frac{\mathrm{d}\boldsymbol{v}_p}{\mathrm{d}t} = \boldsymbol{f}^{\leftarrow f} + \boldsymbol{f}^{\leftrightarrow p} \tag{2.5}$$

and

$$\frac{\mathrm{d}\left(\boldsymbol{I}\boldsymbol{\omega}_p\right)}{\mathrm{d}t} = \boldsymbol{T}^{\leftarrow f} + \boldsymbol{T}^{\leftrightarrow p}, \tag{2.6}$$

respectively. Here, $m(=4\pi\rho_p ab^2/3)$ is the particle mass and $\boldsymbol{I}$ is the moment of inertia. On the right-hand sides of these equations, $\boldsymbol{f}^{\leftarrow f}$ and $\boldsymbol{T}^{\leftarrow f}$ denote the force and torque acting on a particle by the surrounding fluid, respectively, and $\boldsymbol{f}^{\leftrightarrow p}$ and $\boldsymbol{T}^{\leftrightarrow p}$ denote the interaction force and torque between particles, respectively. In the present DNS, since we neglect gravity, the energy is injected only by the external force (2.3) on fluid.

We treat particle-fluid interaction by an immersed boundary method proposed by Uhlmann (2005) to evaluate forces $\boldsymbol{f}^{\leftarrow p}$ in (2.1) and $\boldsymbol{f}^{\leftarrow f}$ in (2.5) and torque $\boldsymbol{T}^{\leftarrow f}$ in (2.6). On the other hand, we treat particle-particle interaction by the discrete element method (DEM) to evaluate $\boldsymbol{f}^{\leftrightarrow p}$ in (2.5) and $\boldsymbol{T}^{\leftrightarrow p}$ in (2.6). In the present DEM, similarly to Moriche *et al.* (2023), we consider only the normal component of the contact force due to elastic collisions, which is proportional to the squared overlap distance.

To simulate the rotational motion governed by (2.6), we employ the method used by Moriche, Uhlmann & Dušek (2021), where we introduce the frame attached to each particle with its origin being the particle centre and with axes parallel to the particle's major and minor axes. Using the angular velocity $\boldsymbol{\omega}'_p$ in this frame, we can rewrite (2.6) as

$$\boldsymbol{I}'\frac{\mathrm{d}\boldsymbol{\omega}'_p}{\mathrm{d}t} + \boldsymbol{\omega}'_p \times \boldsymbol{I}'\boldsymbol{\omega}'_p = \boldsymbol{R}\left(\boldsymbol{T}^{\leftarrow f} + \boldsymbol{T}^{\leftrightarrow p}\right). \tag{2.7}$$

Here, $\boldsymbol{I}'$ is the principal moment of inertia,

$$\boldsymbol{I}' = \beta \begin{pmatrix} 2mb^2/5 & 0 & 0 \\ 0 & m(a^2+b^2)/5 & 0 \\ 0 & 0 & m(a^2+b^2)/5 \end{pmatrix} \tag{2.8}$$

and $\boldsymbol{R}$ is the rotation matrix between the two frames expressed as

$$\boldsymbol{R} = \begin{pmatrix} q_0^2+q_1^2-q_2^2-q_3^2 & 2\,(q_1q_2+q_0q_3) & 2\,(q_1q_3-q_0q_2) \\ 2\,(q_1q_2-q_0q_3) & q_0^2-q_1^2+q_2^2-q_3^2 & 2\,(q_2q_3+q_0q_1) \\ 2\,(q_1q_3+q_0q_2) & 2\,(q_2q_3-q_0q_1) & q_0^2-q_1^2-q_2^2+q_3^2 \end{pmatrix} \tag{2.9}$$

with quaternion $\boldsymbol{q} = (q_0, q_1, q_2, q_3)$. In terms of $\boldsymbol{\omega}'_p = (\omega'_{px}, \omega'_{py}, \omega'_{pz})$, we can express the temporal evolution of the quaternion as

$$\frac{\mathrm{d}\boldsymbol{q}}{\mathrm{d}t} = \frac{1}{2} \begin{pmatrix} q_0 & -q_1 & -q_2 & -q_3 \\ q_1 & q_0 & -q_3 & q_2 \\ q_2 & q_3 & q_0 & -q_1 \\ q_3 & -q_2 & q_1 & q_0 \end{pmatrix} \begin{pmatrix} 0 \\ \omega'_{px} \\ \omega'_{py} \\ \omega'_{pz} \end{pmatrix}. \tag{2.10}$$

Thus, we solve (2.7) and (2.10) instead of (2.6) for the rotational motion of particles. We numerically integrate (2.5), (2.7) and (2.10) with the Euler method for the particle-particle interaction terms and the second-order Adams–Bashforth method for the other terms. We solve the governing equations for fluid and particles alternately so that we can treat coupled motion of fluid and particles.

Note that we have introduced in (2.8) an artificial coefficient β to express the inhomogeneous distribution of mass density in a particle; $\beta = 1$ corresponds to the homogeneous density distribution. By the introduction of β, we can discuss whether the rotation of particles is important or not in turbulence modulation (see § 3.3).

2.2. *Particle parameters*

We examine interaction between prolate spheroidal particles and the statistically stationary turbulence with properties given in table 1. Then, the particles are characterised by four parameters: the equivalent diameter $D_* = 2(ab^2)^{1/3}$, which is defined as (1.7), the aspect ratio $\chi = a/b$ ($\chi \geqslant 1$), the mass density ratio $\gamma = \rho_p/\rho_f$ between the particle and fluid, and coefficient β in (2.8) determining the inertial moment. We fix the particle volume fraction $\Lambda = (4\pi ab^2 N_p/3L_0^3)$, where N_p is the number of particles, at 6.0×10^{-3}, which is slightly more dilute than the system in our previous study (Oka & Goto 2022). Note that since Λ is fixed, the number N_p of particles increases as D_* decreases.

First, we describe particle parameters with homogeneous mass density ($\beta = 1$). We consider the two cases with relatively small diameters $D_*/L = 0.16$ and 0.24 (i.e. $D_*/\eta = 7.5$ and 11). Here, we use the values of L and η in the single-phase flow. Then, we change the aspect ratio ($\chi = 1$, 3, 5 and 7) and mass density ratio ($\gamma = 8$, 32, 128 and 512) to examine 32 cases in total. We show results on the basis of the Stokes number (1.1) instead of γ. The Stokes number St denotes the ratio between the velocity relaxation time,

$$\tau_p = \begin{cases} \dfrac{2\gamma b^2}{9\nu} & (\text{for } \chi = 1), \\ \dfrac{2\gamma b^2 f(\chi)}{9\nu} & (\text{for } \chi > 1), \end{cases} \tag{2.11}$$

(*a*) $D_*/L = 0.16$

χ	$2a/L$	$2a/\eta$	$2b/L$	$2b/\eta$	γ	St	β	St_r	N_p
1	0.16	7.6	0.16	7.6	8	1.9	1	2.0	422
1	0.16	7.6	0.16	7.6	32	7.4	1	8.0	422
1	0.16	7.6	0.16	7.6	128	30	1	32	422
1	0.16	7.6	0.16	7.6	512	119	1	127	422
3	0.33	16	0.11	5.2	8	1.7	1	2.0	422
3	0.33	16	0.11	5.2	32	6.7	1	8.2	422
3	0.33	16	0.11	5.2	128	27	1	33	422
3	0.33	16	0.11	5.2	512	107	1	131	422
5	0.47	22	0.093	4.4	8	1.5	1	1.9	422
5	0.47	22	0.093	4.4	32	5.9	1	7.6	422
5	0.47	22	0.093	4.4	128	24	1	31	422
5	0.47	22	0.093	4.4	512	95	1	122	422
7	0.58	28	0.083	4.0	8	1.3	1	1.8	422
7	0.58	28	0.083	4.0	32	5.4	1	7.1	422
7	0.58	28	0.083	4.0	128	22	1	28	422
7	0.58	28	0.083	4.0	512	86	1	114	422
7	0.58	28	0.083	4.0	32	5.4	1/4	1.8	422
7	0.58	28	0.083	4.0	32	5.4	1/16	0.45	422
7	0.58	28	0.083	4.0	512	86	1/16	7.1	422
7	0.58	28	0.083	4.0	512	86	1/64	1.8	422

(*b*) $D_*/L = 0.24$

χ	$2a/L$	$2a/\eta$	$2b/L$	$2b/\eta$	γ	St	β	St_r	N_p
1	0.24	11	0.24	11	8	4.2	1	3.4	125
1	0.24	11	0.24	11	32	17	1	14	125
1	0.24	11	0.24	11	128	67	1	54	125
1	0.24	11	0.24	11	512	268	1	217	125
3	0.50	23	0.17	7.8	8	3.8	1	3.5	125
3	0.50	23	0.17	7.8	32	15	1	14	125
3	0.50	23	0.17	7.8	128	60	1	56	125
3	0.50	23	0.17	7.8	512	241	1	223	125
5	0.70	33	0.14	6.6	8	3.4	1	3.3	125
5	0.70	33	0.14	6.6	32	13	1	13	125
5	0.70	33	0.14	6.6	128	54	1	52	125
5	0.70	33	0.14	6.6	512	215	1	208	125
7	0.88	41	0.13	5.9	8	3.1	1	3.0	125
7	0.88	41	0.13	5.9	32	12	1	12	125
7	0.88	41	0.13	5.9	128	49	1	48	125
7	0.88	41	0.13	5.9	512	195	1	194	125
7	0.88	41	0.13	5.9	32	12	1/4	3.0	125
7	0.88	41	0.13	5.9	32	12	1/16	0.76	125
7	0.88	41	0.13	5.9	512	195	1/16	12	125
7	0.88	41	0.13	5.9	512	195	1/64	3.0	125

Table 2. Particle parameters for (*a*) $D_*/L = 0.16$ (RUN384 in table 1) and (*b*) $D_*/L = 0.24$ (RUN256).

where we define $\xi = \sqrt{\chi^2 - 1}$ and $f(\chi) = \chi \ln(\chi + \xi)/\xi$, of the spheroidal particles (Shapiro & Goldenberg 1993) and the integral time T of single-phase turbulence. Note that (2.11) is a reference particle relaxation time estimated by assuming the Stokes drag. We list in table 2 the parameters of particles. The number of grid points in DNS is

$N^3 = 384^3$ for $D_*/L = 0.16$ and $N^3 = 256^3$ for $D_*/L = 0.24$ to ensure $D_*/\Delta x = 12$, where Δx $(= L_{box}/N)$ is the grid width.

Next, we explain the additional particle parameter β, which expresses the inhomogeneous mass density distribution inside each particle. Note that, by changing the value of β in (2.8), we can change the particles' ability of rotation. When $\beta = 1$, the mass density is homogeneously distributed; whereas when $\beta < 1$, it is larger around the particle centre and such a particle can rotate more easily than the one with $\beta = 1$. Since β cannot be arbitrarily large, we examine particles with $\beta \leqslant 1$. To quantify the rotational ability of particles, we define the rotational Stokes number as

$$St_r = \frac{\tau_r}{\tau_{D_*}}\,, \tag{2.12}$$

which denotes the ratio between the relaxation time (Jayaram *et al*. 2023),

$$\tau_r = \begin{cases} \dfrac{3\beta}{10}\,\tau_p & (\text{for } \chi = 1), \\ \dfrac{9\beta}{40}\,\dfrac{c_0 + \chi^2 c_1}{f(\chi)}\,\tau_p & (\text{for } \chi > 1), \end{cases} \tag{2.13}$$

of the particle tumbling motion and the turnover time, $\tau_{D_*}(=\epsilon_0^{-1/3} D_*^{2/3})$, of vortices at scale D_*. In (2.13), c_0 and c_1 are

$$c_0 = \frac{2\chi^2\xi + \chi\,\ln(\chi - \xi) - \chi\,\ln(\chi + \xi)}{2\xi^3} \quad \text{and} \quad c_1 = \frac{-2\xi - \chi\,\ln(\chi - \xi) + \chi\,\ln(\chi + \xi)}{\xi^3}\,, \tag{2.14}$$

respectively. The rotational Stokes number St_r represents the ability for the particles to follow the swirling of vortices with size D_*. In the present study, in addition to the 32 kinds of particles with homogeneous density ($\beta = 1$), we simulate particles with different values of St_r corresponding to $\beta = 1/4$, $1/16$ and $1/64$ in the eight cases of the most elongated ($\chi = 7$) (see table 2).

Before showing the results, we recall that turbulence driven by (2.3) has mean flow. In Appendix A, we show that particles with the dilute volume fraction do not significantly change the average kinetic energy K of the mean flow or the integral length L. These features are important because they are assumed in (1.4), which is required to derive the formula (1.5) of attenuation rate. In the next section, we demonstrate that (1.5) holds even for anisotropic particles.

3. Results

3.1. *Attenuation of turbulent kinetic energy*

In the following analysis, we evaluate statistics by taking temporal average over approximately $250T$. The error bars in the following figures indicate the standard deviation. We first show results for particles with homogeneous mass density distribution ($\beta = 1$).

Figure 1 shows the St-dependence of the temporal average K' of turbulent kinetic energy normalised by the value K'_0 for the single-phase flow. The blue smaller symbols are results for $D_*/L = 0.16$ and black larger ones are for $D_*/L = 0.24$. The shape of symbols with different ellipticity represents the particle shape with different aspect ratios $\chi = 1$, 3, 5 and 7. Note that the shape of the symbols is schematic. We see in this figure that, for given D_* and χ, turbulent kinetic energy is attenuated more significantly for larger St. This tendency is common in both cases with spherical particles (circles in the figure)

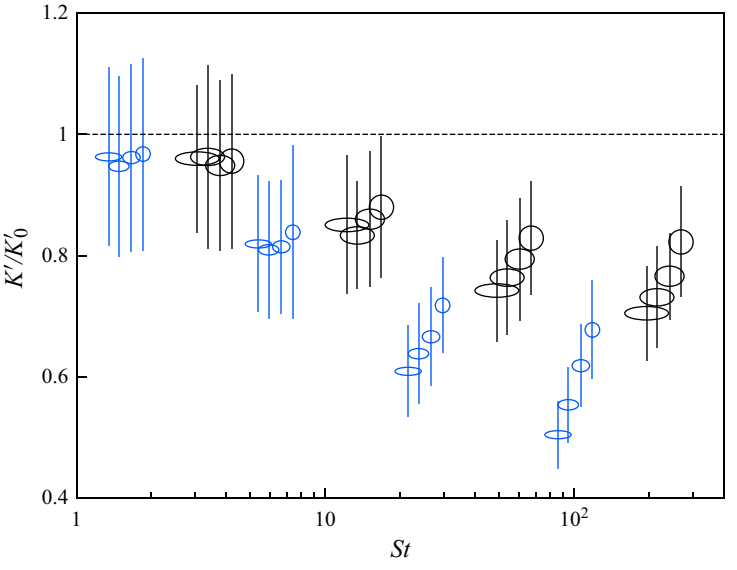

Figure 1. Average turbulent kinetic energy K' normalised by the value K'_0 for the single-phase flow as a function of St. Blue smaller symbols are results for $D_*/L = 0.16$ and black larger ones are for $D_*/L = 0.24$. The shape of symbols with different ellipticity represents the aspect ratios ($\chi = 1$, 3, 5 and 7) of particles; note that the shape of symbols is schematic and different from the examined spheroids. Error bars indicates the standard deviation.

and with spheroidal ones (ellipses). We therefore conclude that the largeness of St is a necessary condition for turbulence attenuation irrespective of particle shape.

Our previous study (Oka & Goto 2022) for spherical particles demonstrated that shedding vortices behind particles play important roles in turbulence attenuation because they are relevant for the additional dissipation rate ϵ_p. Similar vortices can be observed around spheroidal particles with large St. Figures 2(a) and 2(b) show vortices (blue objects) identified by isosurfaces of the enstrophy and particles (yellow ones). The particles shown in these two panels have the same size ($D_*/L = 0.16$) and aspect ratio ($\chi = 7$) but different values of the Stokes number: (a) $St = 1.3$ and (b) 86. Panels (c) and (d) show a cross-section of panels (a) and (b), respectively, which is perpendicular to the four columnar vortices driven by external force (2.3). Since the most energetic large-scale flow is parallel to this cross-section, we can easily judge whether or not shedding vortices exist by the enstrophy indicated by the background colour in panels (c) and (d). We see in the visualisations of panel (a, c) for $St = 1.3$ (and supplementary movie 1 available at https://doi.org/10.1017/jfm.2025.137) that the enstrophy is distributed independently of particles. This implies that vortices are generated through energy cascade even in the presence of particles, and there is no additional energy dissipation around them in this case with small St. In contrast, vortices are created behind particles with larger Stokes number ($St = 86$) as shown in figure 2(b,d). Figure 2(e) shows the magnification of a subdomain of figure 2(b). It is clear in figure 2(b,d,e) that elongated vortices are shed along particles. Since these shedding vortices are as small as 10η, they are almost immediately dying due to viscous effects. This additional energy dissipation in the shedding vortices leads to the reduction in part of the cascading energy flux, and consequently turbulent kinetic energy is attenuated. This is consistent with the physical picture described in the introduction.

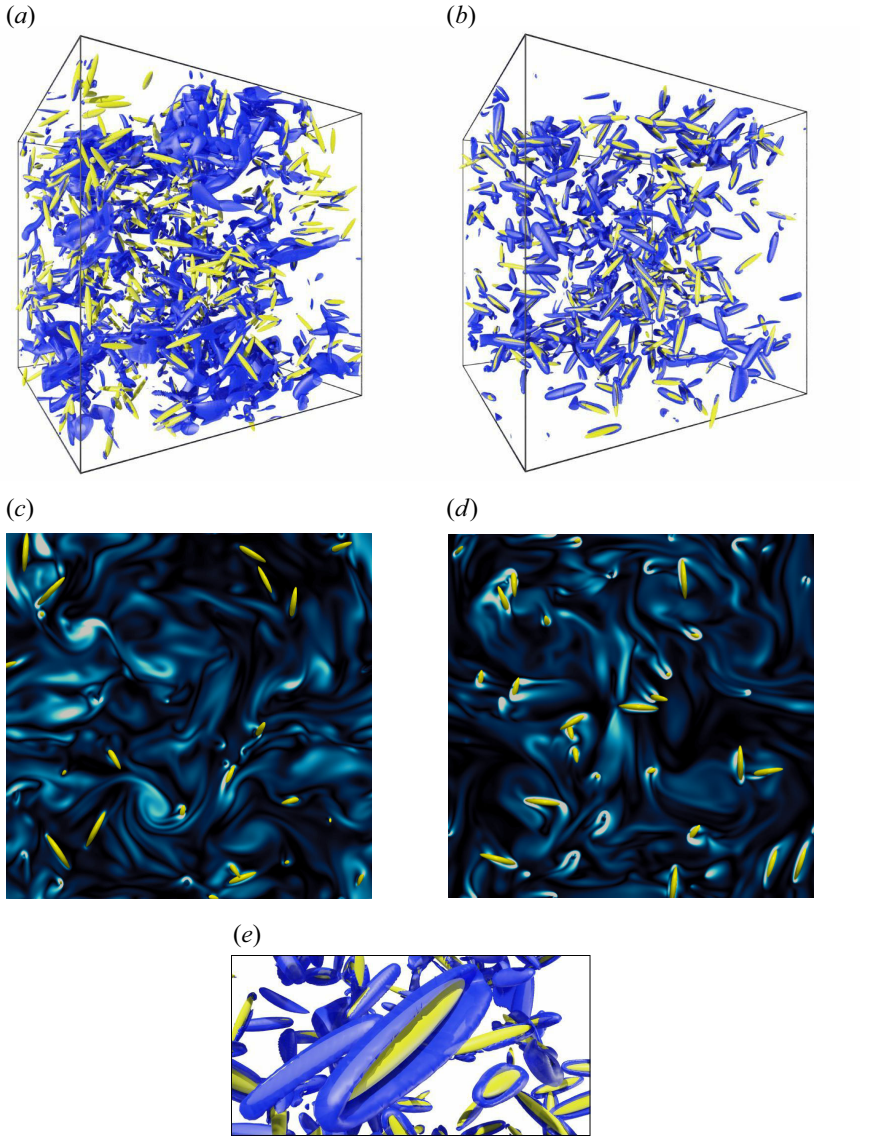

Figure 2. Visualisation of vortices (blue objects) identified by isosurfaces of enstrophy and spheroidal particles (yellow ones) with (*a*) $St = 1.3$ and (*b*) $St = 86$. Particle size is $D_*/L = 0.16$ and aspect ratio is $\chi = 7$. Panels (*c*) and (*d*) show $z = 0$ planes of panels (*a*) and (*b*), respectively. The background colour indicates the magnitude of the enstrophy (lighter colours show the larger value). Panel (*e*) shows a subdomain of panel (*b*). See also supplementary movie 1.

Figure 1 also shows that the attenuation rate of turbulent kinetic energy depends on not only St, but also equivalent diameter D_* and aspect ratio χ. More specifically, for given St, turbulent kinetic energy is attenuated more significantly for smaller D_* or larger χ.

Concerning particle size D_*, we can explain its effect on the turbulence attenuation by the same argument as for spherical particles (Oka & Goto 2022); that is, smaller particles can produce larger additional energy dissipation rate ϵ_p per unit mass because it is inversely proportional to D_* [see (1.6)]. We emphasise that this statement is valid under the condition that the volume fraction Λ is constant.

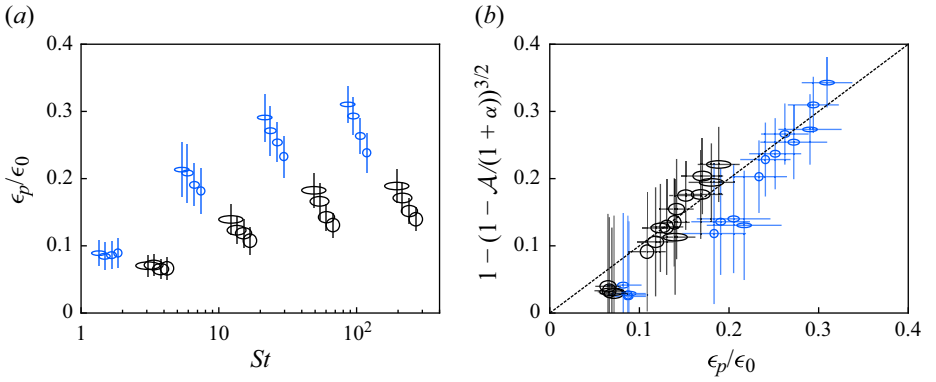

Figure 3. (*a*) Energy dissipation rate ϵ_p evaluated by (3.1) around particles as a function of St. (*b*) Numerical verification of (1.5), which is indicated by the dashed straight line. The symbols are the same as in figure 1.

However, concerning aspect ratio χ, it is unclear whether we can describe the χ-dependence solely in terms of the additional energy dissipation rate ϵ_p around particles. This is a crucial issue because for larger Stokes numbers (say, $St \gtrsim 20$), more elongated particles attenuate turbulence more significantly and the χ-dependence of the attenuation rate is non-negligible (figure 1).

To consider the effect of particle shape, we therefore examine the dependence of ϵ_p on St, D_* and χ. Here, we numerically compute the local average of the energy dissipation rate around each particle as

$$\epsilon_p = \frac{1}{L_{box}^3}\left(\overline{\int_{\Omega_p} \epsilon(\boldsymbol{x}, t)\,\mathrm{d}V} - V_{\Omega_p}\epsilon\right), \tag{3.1}$$

where Ω_p denotes the spheroidal shell between the particle surface and another spheroid with the major and minor radii being $a + 3D_*/4$ and $b + 3D_*/4$, respectively, and V_{Ω_p} denotes the volume of Ω_p. The first term on the right-hand side of (3.1) denotes the local energy dissipation rate around particles. However, since this quantity includes the dissipation rates due to both the shedding vortices and vortices generated by energy cascade, we subtract the latter contribution expressed by the second term so that we can estimate the additional dissipation rate. Here, note that ϵ in the second term of (3.1) is the average quantity in time and space (i.e. $\epsilon = \overline{\langle\epsilon(\boldsymbol{x}, t)\rangle}$).

Figure 3(*a*) shows the thus-evaluated ϵ_p, normalised by the energy dissipation rate ϵ_0 in the single-phase flow, as a function of St. We see that ϵ_p gets larger for (i) larger Stokes number St, (ii) larger aspect ratio χ and (iii) smaller equivalent diameter D_*. These behaviours are similar to those of turbulence attenuation rate shown in figure 1, implying that the turbulence attenuation rate relates to ϵ_p. In fact, plotting in figure 3(*b*) all the data according to (1.5), we can confirm that (1.5) holds irrespective of St, D_* and χ.

In summary, (1.5) describing turbulence attenuation is valid even for the anisotropic particles. For the estimation of ϵ_p required for (1.5), we have numerically evaluated it by (3.1). This direct evaluation however lacks a concrete relevance of ϵ_p to particle properties such as St, D_* and χ. On the other hand, for spheres, ϵ_p is described in terms of the translational relative velocity Δu and particle diameter D according to (1.6). In the next subsection, we generalise (1.6) for anisotropic particles.

3.2. *Estimation of energy dissipation rate due to particles*

To estimate the energy dissipation rate ϵ_p around particles, we first assume that ϵ_p is determined by the translational motion of particles. Then, we can estimate it by using the force F_p acting on a particle:

$$F_p = \frac{1}{2} C_D \rho_f (\Delta u)^2 A \,, \tag{3.2}$$

where C_D is the drag coefficient, $A(=\pi D_*^2/4)$ is the cross-sectional area of a sphere with diameter of D_* and is the translational relative velocity between the particle $\boldsymbol{v}_p$ and its surrounding fluid. Here, denotes the average on the outer surface of the spheroidal shell Ω_p around each particle. Since a particle subjected to F_p inputs energy to flow at the rate of $F_p \Delta u$, the average energy dissipation rate per unit mass in wakes around all particles in the system is expressed as

$$\epsilon_p^\dagger = \frac{3}{4} \Lambda \frac{\langle C_D \Delta u^3 \rangle_p}{D_*} \,. \tag{3.3}$$

This estimation of $\epsilon_p^\dagger$ differs from (1.6) used for spheres by Oka & Goto (2022) because they assumed that C_p is a constant of $O(1)$. For anisotropic particles, it is important to consider the dependence of C_D on the shape of particles as well as flow state surrounding them. In fact, the instantaneous drag coefficient C_D depends on the particle Reynolds number $Re_p = \Delta u D_*/\nu$, aspect ratio χ and angle ϕ between the major axis of the particle and relative velocity. In the present study, to evaluate C_D from Δu and ϕ, we use the expression,

$$C_D(\phi, Re_p) = C_{D,\phi=0} + \left(C_{D,\phi=\pi/2} - C_{D,\phi=0}\right) \sin^2 \phi \,, \tag{3.4}$$

proposed by Sanjeevi, Dietiker & Padding (2022) according to their numerical results. Here, $C_{D,\phi} = (a_1/Re_p + a_2/Re_p^{a_3}) \exp(-a_4 Re_p) + a_5\{1 - \exp(-a_4 Re_p)\}$, with a_i $(i = 1, \ldots, 5)$ being the coefficients depending on χ and ϕ. The values of these coefficients are listed in table 2 of Sanjeevi *et al.* (2022). Figure 4(*a*) shows the χ-dependence of $\langle C_D \rangle_p$ for the case of the smallest particles with the largest St (i.e. $D_*/L = 0.16$ and $\gamma = 512$). For larger χ, $\langle C_D \rangle_p$ gets larger. This implies that $\epsilon_p^\dagger$ is larger for more elongated particles. We have also confirmed similar monotonically increasing trend with respect to χ for the other particles. It is not trivial whether (3.4), which is derived for a particle in uniform flow (Sanjeevi *et al.* 2022), gives a good approximation in turbulence. However, the observation in figure 4(*a*) is consistent with the direct evaluation of ϵ_p shown in figure 3(*a*). In addition, the increasing trend of $\langle C_D \rangle_p$ with χ is also consistent with the result for decaying turbulence by Schneiders *et al.* (2019), who explained the trend in terms of particle orientations.

Furthermore, figure 4(*b*) shows the average $\langle \Delta u \rangle_p$ of the relative velocity for all the simulated particles. For given D_* and χ, the relative velocity is larger for larger St, and it tends to approximately u' for $St \gg 1$. This is reasonable because St represents the ability for particles to follow the swirling motion around the largest vortices. Incidentally, although the feature that $\langle \Delta u \rangle_p \to 1.5u'$–$2u'$ for $St \gg 1$ is independent of the kind of external force, the prefactor depends on forcing(see Oka & Goto 2022, figure 6).

Using the numerically evaluated averages of $C_D \Delta u^3$, we estimate the energy dissipation rate $\epsilon_p^\dagger$ around particles by using (3.3). Figure 5(*a*) shows the relation between $\epsilon_p^\dagger$ and ϵ_p. We can observe that $\epsilon_p^\dagger$ well coincides with ϵ_p. This means that the estimation (3.3) accurately quantifies the energy dissipation rate around particles. In other words,

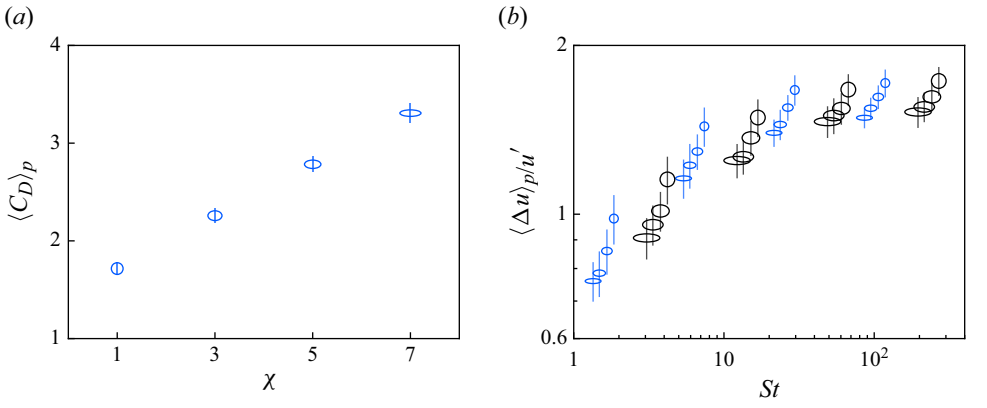

Figure 4. (*a*) Averaged drag coefficient C_D for particles with $\gamma = 512$ and $D_*/L = 0.16$ as a function of χ. (*b*) Relative velocity normalised by u' as a function of St. Symbols are the same as in figure 1.

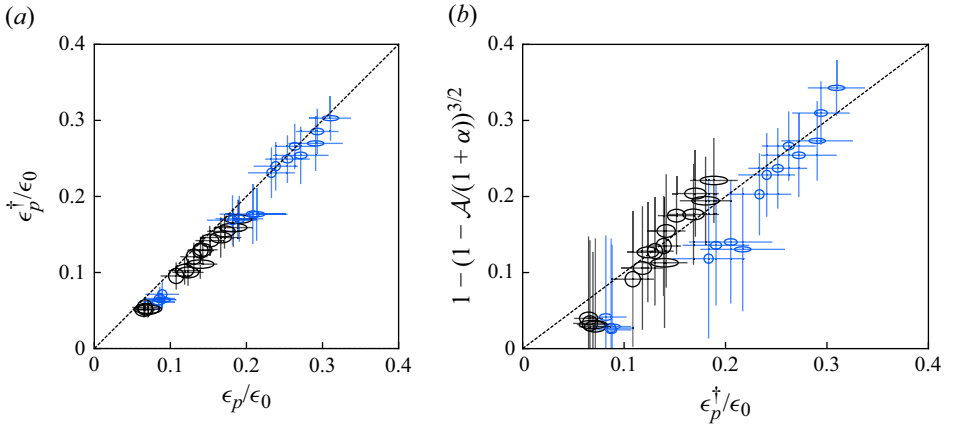

Figure 5. (*a*) Comparison of the energy dissipation rates between the numerical evaluation ϵ_p using (3.1) and estimation $\epsilon_p^\dagger$ using (3.3). Both values are normalised by the energy dissipation rate ϵ_0 in the single-phase flow. (*b*) Numerical verification of (1.5), where we use the value $\epsilon_p^\dagger$, instead of ϵ_p, for the energy dissipation rate. The dashed lines in the both panels show linear lines with a slope of 1. Symbols are the same as in figure 1.

as explicitly demonstrated in figure 5(*b*), we can use the estimation $\epsilon_p^\dagger$ in place of ϵ_p in (1.5) to describe the turbulence attenuation rate in the case for spheroidal particles.

Although overall data shown in figure 5(*b*), as well as figure 3(*b*), support (1.5) and (3.3), we observe systematic deviation from the diagonal line in these figures. More concretely, for both sets of different particle diameters (blue and black symbols represent $D_* = 0.16L$ and $0.24L$, respectively), the deviation is larger for smaller St (i.e. smaller ϵ_p) cases. This is because, when $St \lesssim 10$, the velocity difference between particles and fluid is not determined only by the translational motion as will be discussed in the next subsection.

We emphasise the importance of the estimation (3.3) of ϵ_p because it tells us that the energy dissipation rate around particles gets larger for larger Δu, larger C_D or smaller D_* in a quantitative manner. In particular, since $\Delta u = O(u')$ for $St \gg 1$ (figure 4*b*), we may predict $\epsilon_p^\dagger$, and therefore $\mathcal{A}$, as a function of particle shape parameters D_* and χ. We also emphasise that the estimation (3.3) is non-trivial because we estimate ϵ_p by considering only translational motion of particles. In other words, we have neglected contribution from

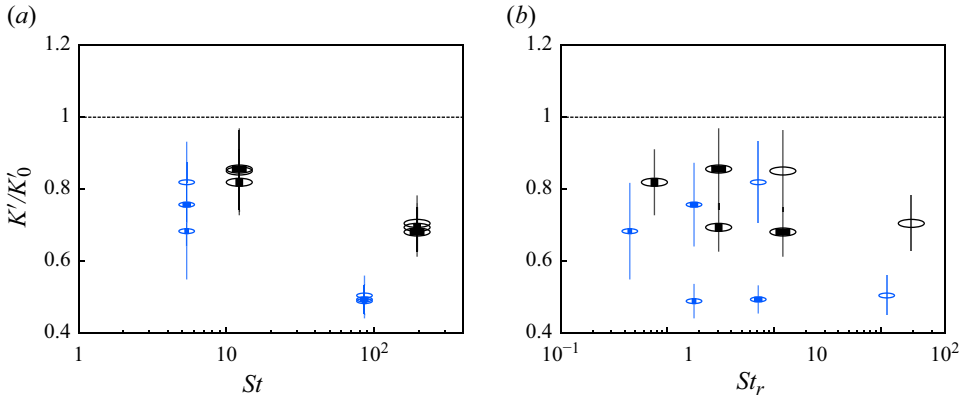

Figure 6. Temporal average K' of turbulent kinetic energy normalised by the value K'_0 for the single-phase flow as functions of (*a*) St and (*b*) St_r. The open symbols indicate results for particles with homogeneous mass density with the same equivalent diameters ($D_*/L = 0.16$ and 0.24) and aspect ratio ($\chi = 7$), but different Stokes numbers. The partially filled ones indicate results for particles with different values of the inertial moment; the width of the filled part of symbols is narrower for smaller β.

particle rotation in (3.3). As quantitatively demonstrated by Schneiders *et al*. (2019) for decaying turbulence, in fact, the contribution to ϵ_p from translational motion of particles dominates those from their rotations and fluid acceleration. We further discuss effects of particle rotation in the next subsection.

3.3. *Effects of the rotation of particles*

As demonstrated in figure 5(*b*), the degree of turbulence attenuation is described by additional energy dissipation rate $\epsilon_p^\dagger$ around particles. We have also shown in figure 5(*a*) that $\epsilon_p^\dagger$ can be quantified by the translational relative velocity between particles and fluid. In this subsection, we verify that the rotation of particles is less important on the turbulence attenuation when $St \gg 1$. To this end, we simulate different kinds of particles, which have inhomogeneous distribution of mass density inside, with different values of β ($= 1/4$, $1/16$ and $1/64$) for the inertial moment (see the second row from the right in table 2). The rotational Stokes number St_r of these particles is much smaller than particles with homogeneous density, which means that the particles are more likely to rotate together with circulation in vortices of size D_*. In such a case, the relative velocity, and therefore the energy dissipation rate ϵ_p around particles, might be affected by difference in the swirling of vortices and tumbling of particles.

Figure 6 shows the ratio K'/K'_0 of turbulent kinetic energy in single-phase flow and turbulence with particles with smaller values of β as functions of St in panel (*a*) and St_r in panel (*b*). The partially filled symbols indicate results for particles with inhomogeneous mass density ($\beta \neq 1$), while open symbols show those for particles with $\beta = 1$. This figure shows that when St is sufficiently large (say, $St \gtrsim 10$), even if St_r is significantly different, the degree of the attenuation is almost identical when D_*/L, St and χ are the same. This implies that the effect of the rotation for ϵ_p is negligible and we can estimate the energy dissipation rate by (3.3) for large-St particles. This result is consistent with those by Schneiders *et al*. (2019) and explained as follows. Since the rotational relative velocity Δu_r is determined by swirls of vortices with size D_*, it is estimated by $\epsilon^{1/3} D_*^{1/3}$ in the inertial range of turbulence. If St is sufficiently large, this cannot be larger

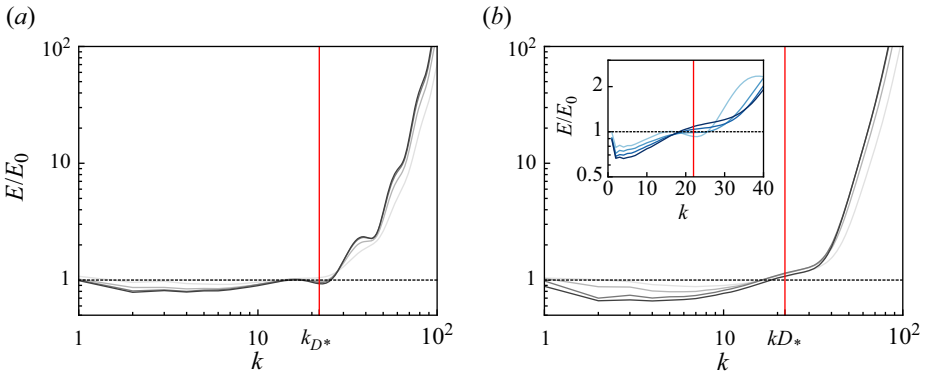

Figure 7. Energy spectra E normalised by the value E_0 in the single-phase flow as a function of the wavenumber k for (a) spheres ($\chi = 1$) and (b) spheroids for $\chi = 7$ with $D_*/L = 0.24$. Darker lines show larger St. The red vertical line represents the wavenumber $k_{D_*} = 2\pi/D_*$ corresponding to the particle diameter. The inset in panel (b) shows results (close-up around k_{D*}) for particles with $\gamma = 512$ and $D_*/L = 0.24$ but different aspect ratios χ. Darker blue lines show larger χ.

than the translational relative velocity $\Delta u (\approx u')$ because $u' \approx \epsilon^{1/3} L^{1/3}$ and, therefore, $\Delta u_r / \Delta u \approx (D_*/L)^{1/3} < 1$.

It is also interesting to observe in figure 6 that the attenuation rate depends on St_r for the case with the smallest value of St ($= 5.4$) indicated by the small blue symbols. This implies that when $1 \lesssim St \lesssim 10$, the attenuation occurs due to energy dissipation in shedding vortices created by not only translational but also rotational motion. Therefore, the assumption for the estimation (3.3) of ϵ_p is violated, which may lead to deviations in figures 2(b) and 4(b) of the data for $St \lesssim 10$.

3.4. *Modulation of energy spectrum*

Before concluding this article, we investigate the scale-dependent modulation of turbulent kinetic energy. In physical space, as shown in figure 2, a key ingredient of the turbulence attenuation is shedding vortices in the wake behind particles because they dissipate the energy at particle scale D_*. More precisely, because of the additional energy dissipation, such vortices reduce the cascading energy flux in scales between integral length L and particle size D_*, whereas they augment turbulence at scales smaller than D_*. This is quantitatively confirmed in figure 7, which shows the energy spectrum $E(k)$, normalised by the value $E_0(k)$ in the single-phase flow, for spherical particles ($\chi = 1$) in panel (a) and most elongated spheroidal ones ($\chi = 7$) in panel (b). The darker lines are results with larger St. The wavenumber $k_{D_*} (= 2\pi/D_*)$ corresponding to particle size D_* is indicated by the red line. In both cases of spheres and spheroids, we observe that the energy spectrum is indeed attenuated in the range $k \lesssim k_{D_*}$ and augmented for $k \gtrsim k_{D_*}$. This observation is similar to previous results (ten Cate *et al.* 2004; Yeo *et al.* 2010; Gao *et al.* 2013; Wang *et al.* 2014) for spherical particles and consistent with the above-mentioned turbulence attenuation mechanism. Incidentally, the cross-over ($E/E_0 \gtrless 1$) of the modulation for spheroids (figure 7b) is obscurer than that for spheres owing to the effect of the length scale separation between major and minor radii. We can confirm this in the inset of figure 7(b), which shows the dependence of E/E_0 on the aspect ratio χ ($= 1$, 3, 5 and 7). The cross-over becomes indeed obscurer for larger χ.

4. Conclusions

We can describe the attenuation of turbulence by solid particles in a periodic cube in terms of the additional energy dissipation rate ϵ_p in the wake behind particles. More precisely, by considering that the cascading energy flux is reduced by ϵ_p, we can derive (1.5) for the attenuation rate $\mathcal{A}$ defined as (1.2). Although (1.5) was verified for turbulence attenuation due to spherical particles (Oka & Goto 2022), we have shown in the present study the numerical evidence that the formula holds even for spheroidal particles and the method how to estimate ϵ_p for such anisotropic particles. In the following, we summarise concrete conclusions.

As demonstrated in figure 1, turbulent kinetic energy is more reduced by particles with larger Stokes number St, (1.1), smaller size D_*, (1.7), or larger aspect ratio χ because ϵ_p gets larger for particles with these properties (figure 3*a*) when the volume fraction Λ of particles is kept constant. Incidentally, although we speculate that ϵ_p is proportional to Λ for fixed D_* because of (1.6), its numerical verification is left for a future study. Figure 3(*b*) shows that once we estimate ϵ_p, we can estimate $\mathcal{A}$ through (1.5). This is the first main conclusion and it implies that, similarly to the case with spherical particles, the key quantity is ϵ_p.

Next, we have shown that ϵ_p can be estimated by (3.3), which depends on St, D_* and χ. For given D_* and χ, ϵ_p is larger for larger St because the average relative velocity Δu is larger (figure 4*b*). Therefore, according to (3.3), ϵ_p takes larger values in the shedding vortices visualised in figure 2(*b*,*d*,*e*) in the case with large St, which leads to larger $\mathcal{A}$ because of (1.5). Equation (3.3) also explains that ϵ_p, and therefore $\mathcal{A}$, become larger for smaller D_*. Here, it is important that the estimation $\epsilon_p^\dagger$ of the dissipation rate, (3.3), depends on the drag coefficient C_D, which is a function of χ, Δu and the angle ϕ between the major axis of particle and relative velocity. We have numerically estimated the average of C_D (figure 4*a*) to evaluate ϵ_p by (3.3) to show that the obtained value of $\epsilon_p^\dagger$ almost perfectly coincides with the direct estimation of ϵ_p (figure 5*a*). Therefore, as demonstrated in figure 5(*b*), we can use $\epsilon_p^\dagger$ in place of ϵ_p in (1.5).

These results lead to the second conclusion that we can predict the attenuation rate by (1.5) through (3.3). In fact, when St is sufficiently large, particles acquire their kinetic energy from the largest vortices, and the cascading energy flux is reduced. This explains the reduction of the averaged energy spectrum $E(k)$ in the wavenumber range $k \lesssim k_{D_*}$ (figure 7). On the other hand, the shedding vortices augment $E(k)$ for $k \gtrsim k_{D_*}$ corresponding to length scales smaller than D_*. Since these behaviours of $E(k)$ for the anisotropic particles are similar to those for spherical ones (ten Cate *et al*. 2004; Yeo *et al.* 2010; Gao *et al.* 2013; Wang *et al*. 2014), we conclude that the physical mechanism of the attenuation is also common.

We emphasise that we neglect effects of rotational motion of particles for ϵ_p in (3.3). This is justified because the relative velocity between fluid and particles due to their rotation cannot be larger than the swirling velocity $\epsilon^{1/3} D_*^{1/3}$ of vortices with particle size $D_* (< L)$, which is smaller than the translational relative velocity of $O(u')$ $(\approx \epsilon^{1/3} L^{1/3})$ for large-St particles. Although for small-St particles, the rotation of particles can affect the relative velocity, this cannot be pronounced in the examined turbulence at the moderate Reynolds number ($R_\lambda \approx 50$). This is explicitly verified in figure 6, which shows that the attenuation rate is independent of the inertial moment of particles for large-St particles. We therefore conclude for the examined large-St cases that the reason why more elongated particles attenuate turbulence more significantly is not their rotational motion, but it is due

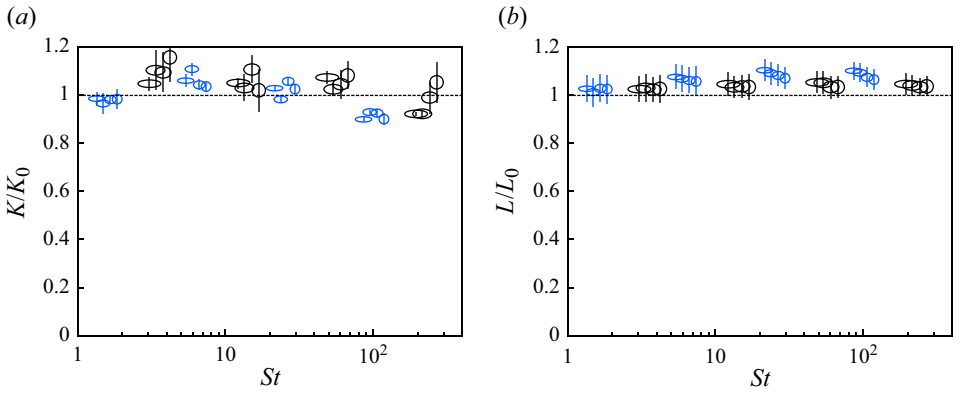

Figure 8. Average of (a) kinetic energy K of the mean flow and (b) integral length L normalised by the values K_0 and L_0 for the single-phase flow, respectively, as a function of St. The symbols are the same as in figure 1.

to the fact that ϵ_p gets larger because smaller vortices are more likely to be shed from more elongated particles.

Funding. This study was partly supported by the JSPS Grants-in-Aid for Scientific Research 20H02068 and 23K13253. The DNS were conducted on the supercomputer Fugaku through the HPCI System Research Projects (hp220232 and hp230288) and the Plasma Simulator under the auspices of the NIFS Collaboration Research Program (NIFS22KISS010).

Supplementary movies. Supplementary movies are available at https://doi.org/10.1017/jfm.2025.137.

Declaration of interests. The authors report no conflict of interest.

Appendix A. Verification of the assumptions for (1.4)

For the estimation of the energy flux ϵ_c in (1.4), which is required for (1.5), we have assumed $K \approx K_0$ and $L \approx L_0$. To numerically verify these assumptions, we show in figure 8(a) the average kinetic energy K of the mean flow and in figure 8(b) the integral length normalised by those (K_0 and L_0) in the single-phase flow, respectively. We can confirm that K/K_0 and L/L_0 are approximately unity regardless of the particle properties. Although Chiarini *et al.* (2024) showed that the mean velocity field can be significantly modulated in the case with a large volume fraction of particles, this is not the case in the dilute regime investigated in the present study. It is also worth mentioning that heavy particles with $St \gtrsim 1$ can be swept out by the largest-scale stationary vortices (Oka & Goto 2021). Therefore, if we consider a denser case, particle clustering can affect the statistics of turbulence modulation.

References

Ardekani, M.N. & Brandt, L. 2019 Turbulence modulation in channel flow of finite-size spheroidal particles. *J. Fluid Mech.* **859**, 887–901.

Balachandar, S. & Eaton, J.K. 2010 Turbulent dispersed multiphase flow. *Annu. Rev. Fluid Mech.* **42** (1), 111–133.

Balachandar, S., Peng, C. & Wang, L.-P. 2024 Turbulence modulation by suspended finite-sized particles: toward physics-based multiphase subgrid modeling. *Phys. Rev. Fluids* **9** (4), 044304.

Bellani, G., Byron, M.L., Collignon, A.G., Meyer, C.R. & Variano, E.A. 2012 Shape effects on turbulent modulation by large nearly neutrally buoyant particles. *J. Fluid Mech.* **712**, 41–60.

Bordoloi, A.D. & Variano, E. 2017 Rotational kinematics of large cylindrical particles in turbulence. *J. Fluid Mech.* **815**, 199–222.

BRANDT, L. & COLETTI, F. 2022 Particle-laden turbulence: progress and perspectives. *Annu. Rev. Fluid Mech.* **54** (1), 159–189.
CANNON, I., OLIVIERI, S. & ROSTI, M.E. 2024 Spheres and fibers in turbulent flows at various Reynolds numbers. *Phys. Rev. Fluids* **9** (6), 064301.
CAPONE, A., ROMANO, G.P. & SOLDATI, A. 2015 Experimental investigation on interactions among fluid and rod-like particles in a turbulent pipe jet by means of particle image velocimetry. *Exp. Fluids* **56** (1), 1–15.
CHIARINI, A., CANNON, I. & ROSTI, M.E. 2024 Anisotropic mean flow enhancement and anomalous transport of finite-size spherical particles in turbulent flows. *Phys. Rev. Lett.* **132** (5), 054005.
ELGHOBASHI, S. 1994 On predicting particle-laden turbulent flows. *Appl. Sci. Res.* **52** (4), 309–329.
ESHGHINEJADFARD, A., HOSSEINI, S.A. & THÉVENIN, D. 2017 Fully-resolved prolate spheroids in turbulent channel flows: a lattice Boltzmann study. *AIP Adv.* **7** (9), 095007.
FUJIKI, Y., AWAI, H., MOTOORI, Y. & GOTO, S. 2024 Attraction of neutrally buoyant deformable particles towards a vortex. *Phys. Rev. Fluids* **9** (1), 014301.
GAO, H., LI, H. & WANG, L.-P. 2013 Lattice Boltzmann simulation of turbulent flow laden with finite-size particles. *Comput. Maths Applics.* **65** (2), 194–210.
GORE, R.A. & CROWE, C.T. 1989 Effect of particle size on modulating turbulent intensity. *Intl J. Multiphase Flow* **15** (2), 279–285.
GOTO, S., SAITO, Y. & KAWAHARA, G. 2017 Hierarchy of antiparallel vortex tubes in spatially periodic turbulence at high Reynolds numbers. *Phys. Rev. Fluids* **2** (6), 064603.
GOTO, S. & VASSILICOS, J.C. 2009 The dissipation rate coefficient of turbulence is not universal and depends on the internal stagnation point structure. *Phys. Fluids* **21** (3), 035104.
HOMANN, H. & BEC, J. 2010 Finite-size effects in the dynamics of neutrally buoyant particles in turbulent flow. *J. Fluid Mech.* **651**, 81–91.
JAYARAM, R., JIE, Y., ZHAO, L. & ANDERSSON, H.I. 2023 Dynamics of inertial spheroids in a decaying Taylor–Green vortex flow. *Phys. Fluids* **35** (3), 033326.
LEVY, Y. & LOCKWOOD, F.C. 1981 Velocity measurements in a particle laden turbulent free jet. *Combust. Flame* **40**, 333–339.
LJUS, C., JOHANSSON, B. & ALMSTEDT, A.-E. 2002 Turbulence modification by particles in a horizontal pipe flow. *Intl J. Multiphase Flow* **28** (7), 1075–1090.
LUCCI, F., FERRANTE, A. & ELGHOBASHI, S. 2010 Modulation of isotropic turbulence by particles of taylor length-scale size. *J. Fluid Mech.* **650**, 5–55.
LUCCI, F., FERRANTE, A. & ELGHOBASHI, S. 2011 Is Stokes number an appropriate indicator for turbulence modulation by particles of Taylor-length-scale size? *Phys. Fluids* **23** (2), 025101.
MANDØ, M. 2009 Turbulence modulation by non-spherical particles. *PhD thesis*, Department of Energy Technology, Aalborg University, Aalborg.
MORICHE, M., HETTMANN, D., GARCÍA-VILLALBA, M. & UHLMANN, M. 2023 On the clustering of low-aspect-ratio oblate spheroids settling in ambient fluid. *J. Fluid Mech.* **963**, A1.
MORICHE, M., UHLMANN, M. & DUŠEK, J. 2021 A single oblate spheroid settling in unbounded ambient fluid: a benchmark for simulations in steady and unsteady wake regimes. *Intl J. Multiphase Flow* **136**, 103519.
OKA, S. & GOTO, S. 2021 Generalized sweep-stick mechanism of inertial-particle clustering in turbulence. *Phys. Rev. Fluids* **6** (4), 044605.
OKA, S. & GOTO, S. 2022 Attenuation of turbulence in a periodic cube by finite-size spherical solid particles. *J. Fluid Mech.* **949**, A45.
OLIVIERI, S., CANNON, I. & ROSTI, M.E. 2022 The effect of particle anisotropy on the modulation of turbulent flows. *J. Fluid Mech.* **950**, R2.
PASCHKEWITZ, J., DUBIEF, Y., DIMITROPOULOS, C.D., SHAQFEH, E.S. & MOIN, P. 2004 Numerical simulation of turbulent drag reduction using rigid fibres. *J. Fluid Mech.* **518**, 281–317.
PENG, C., SUN, Q. & WANG, L.-P. 2023 Parameterization of turbulence modulation by finite-size solid particles in forced homogeneous isotropic turbulence. *J. Fluid Mech.* **963**, A6.
SANJEEVI, S.K., DIETIKER, J.F. & PADDING, J.T. 2022 Accurate hydrodynamic force and torque correlations for prolate spheroids from Stokes regime to high Reynolds numbers. *Chem. Engng J* **444**, 136335.
SCHNEIDERS, L., FRÖHLICH, K., MEINKE, M. & SCHRÖDER, W. 2019 The decay of isotropic turbulence carrying non-spherical finite-size particles. *J. Fluid Mech.* **875**, 520–542.
SCHNEIDERS, L., MEINKE, M. & SCHRÖDER, W. 2017 Direct particle-fluid simulation of Kolmogorov-length-scale size particles in decaying isotropic turbulence. *J. Fluid Mech.* **819**, 188–227.
SHAPIRO, M. & GOLDENBERG, M. 1993 Deposition of glass fiber particles from turbulent air flow in a pipe. *J. Aerosol Sci.* **24** (1), 65–87.

SU, W., ZHANG, H., FU, S., XIANG, X. & WANG, L. 2023 Particle-resolved direct numerical simulation of particleladen turbulence modulation with high stokes number monodisperse spheres. *Phys. Fluids* **35** (10), 105120.

TANAKA, T. & EATON, J.K. 2008 Classification of turbulence modification by dispersed spheres using a novel dimensionless number. *Phys. Rev. Lett.* **101** (11), 1–4.

TAYLOR, G.I. 1935 Statistical theory of turbulence. *Proc. R. Soc. Lond. A* **151** (873), 421–444.

TEN CATE, A., DERKSEN, J.J., PORTELA, L.M. & VAN DEN AKKER, H.E.A. 2004 Fully resolved simulations of colliding monodisperse spheres in forced isotropic turbulence. *J. Fluid Mech.* **519**, 233–271.

TSUJI, Y. & MORIKAWA, Y. 1982 LDV measurements of an air-solid two-phase flow in a horizontal pipe. *J. Fluid Mech.* **120**, 385–409.

UHLMANN, M. 2005 An immersed boundary method with direct forcing for the simulation of particulate flows. *J. Comput. Phys.* **209** (2), 448–476.

VOTH, G.A. & SOLDATI, A. 2017 Anisotropic particles in turbulence. *Annu. Rev. Fluid Mech.* **49** (1), 249–276.

WANG, L.-P., AYALA, O., GAO, H., ANDERSEN, C. & MATHEWS, K.L. 2014 Study of forced turbulence and its modulation by finite-size solid particles using the lattice Boltzmann approach. *Comput. Maths Applics.* **67** (2), 363–380.

WANG, Z., XU, C.-X. & ZHAO, L. 2021 Turbulence modulations and drag reduction by inertialess spheroids in turbulent channel flow. *Phys. Fluids* **33** (12), 123313.

YEO, K., DONG, S., CLIMENT, E. & MAXEY, M.R. 2010 Modulation of homogeneous turbulence seeded with finite size bubbles or particles. *Intl J. Multiphase Flow* **36** (3), 221–233.

ZHAO, F., GEORGE, W. & VAN WACHEM, B.G. 2015 Four-way coupled simulations of small particles in turbulent channel flow: the effects of particle shape and Stokes number. *Phys. Fluids* **27** (8), 083301.